



Full Text View

[Volume 29, Issue 2 \(February 1999\)](#)

Journal of Physical Oceanography

Article: pp. 288–303 | [Abstract](#) | [PDF \(237K\)](#)

Lagrangian and Tracer Evolution in the Vicinity of an Unstable Jet

Emmanuel Boss and LuAnne Thompson

School of Oceanography, University of Washington, Seattle, Washington

(Manuscript received August 18, 1997, in final form June 8, 1998)

DOI: 10.1175/1520-0485(1999)029<0288:LATEIT>2.0.CO;2

ABSTRACT

The dynamics of Lagrangian particles and tracers in the vicinity of a baroclinically unstable zonal jet are investigated in a simple two-layer model with an initially quiescent lower layer. The presence of a growing wave induces a particle drift dominated by Stokes drift rather than the contribution of the wave to the mean Eulerian velocity. Stable and unstable waves have zonal Stokes drift with similar meridional structure while only unstable waves possess meridional drift, which is in the direction of increasing meridional wave displacement. Particle dispersion in the upper layer is maximum at critical lines, where the jet and phase speeds are equal. In the lower layer, dispersion is maximum where the wave amplitude is maximum. Zonal mean tracer evolution is formulated as an advection–diffusion equation with an order Rossby number advection and an order-one eddy diffusion. The latter is proportional to two-particle dispersion.

Finite amplitude simulations of the flow reveal that small amplitude theory has predictive value beyond the range for which it is strictly valid. Mixing (as opposed to stirring) is maximum near cat's-eye-like recirculation regions at the critical lines. In the lower layer the pattern of convergence and divergence of the flow locally increases tracer gradients, resulting in stirring yet with a much slower mixing rate than in the upper layer. Meridional eddy diffusion (or particle dispersion) alone is not sufficient for prediction of mixing intensity. Rotation, which is quantified by the cross-correlation of meridional and zonal displacements, must also be present for mixing.

These results are consistent with observations of tracer and floats in the vicinity of the Gulf Stream.

Table of Contents:

- [Introduction](#)
- [Model flow and theoretical](#)
- [Small amplitude results](#)
- [Large-amplitude numerical](#)
- [Discussion and conclusions](#)
- [REFERENCES](#)
- [APPENDIX](#)
- [FIGURES](#)

Options:

- [Create Reference](#)
- [Email this Article](#)
- [Add to MyArchive](#)
- [Search AMS Glossary](#)

Search CrossRef for:

- [Articles Citing This Article](#)

Search Google Scholar for:

- [Emmanuel Boss](#)
- [LuAnne Thompson](#)

Floats and tracers in the ocean have been used by physical oceanographers to infer both the Eulerian structure of the flow field and the mixing geometry associated with the flow. The primary goal of this paper is to study tracer mixing and Lagrangian particle behavior in a baroclinically unstable jet. In addition, we wish to study the link between the kinematics of floats and tracer and the underlying flow field. The geophysical motivation for this work comes from the Gulf Stream, a region in the ocean in which floats have been used intensively. Lagrangian floats and tracer studies (e.g., [Bower et al. 1985](#); [Bower and Rossby 1989](#); [Bower and Lozier 1994](#); [Song et al. 1995](#)) in the Gulf Stream region have highlighted two main characteristics: on the one hand, the Gulf Stream seems to provide a barrier that separates slope water from Sargasso Sea water; while on the other hand, it is an intense area of mixing ([Song et al. 1995](#)). The sharp potential vorticity (PV) gradient observed in the vicinity of the jet has been assigned the role of a barrier to mixing across the jet ([Bower and Lozier 1994](#)), while mixing has been associated with critical (or steering) lines where the phase speed of the meanders matches the zonal jet speed (e.g., [Owens 1984](#); [Bower 1991](#); [Pratt et al. 1995](#)). Likewise, the presence of a critical level¹ has been invoked to explain the enhanced particle dispersion ([Lozier and Bercovici 1992](#)) below the thermocline. Tracer gradients have been found to be smaller at depth ([Bower et al. 1985](#)), consistent with potentially enhanced mixing there ([Bower 1991](#)).

Theoretical studies of stirring and mixing² with application to the Gulf Stream have recently focused on barotropic and equivalent-barotropic quasigeostrophic (QG) jets with stable Rossby wave perturbations. These studies have emphasized the role of critical levels and/or lines as primary locations for mixing. Using several analytical techniques derived from the theory of dynamical systems, tracer mixing or stirring at these locations was quantified ([Samelson 1992](#); [del-Castillo-Negrete and Morisson 1993](#); Rogerson et al. 1996, manuscript submitted to *J. Phys. Oceanogr.*) or qualitatively assessed ([Pratt et al. 1995](#); [Lozier et al. 1997](#)). These treatments have taken advantage of the two-dimensionality of the QG barotropic flow (i.e., the flow can be derived from a streamfunction) and that the wave amplitudes have no, or slow, evolution.

Gulf Stream observations associate growing meander events with strong subsurface flows, indicating the presence of baroclinic instability ([Watts et al. 1995](#)). In addition, the Gulf Stream has a fairly high Rossby number $[U/(g'H)]^{1/2}$ and $\zeta/f \sim 0.5$ ([Kim and Watts 1994](#)), where U is the speed of the stream, g' its reduced gravity, H the thermocline depth, ζ the relative vorticity, and f the Coriolis parameter. This suggests that the effects of baroclinicity, transient waves and mean flows, and high Rossby numbers should be investigated ([Lozier and Bercovici 1992](#); [Pratt et al. 1995](#)).

[Lozier and Bercovici \(1992\)](#) investigated a baroclinically unstable zonal jet in a continuously stratified QG model. The basic-state jet varied only in the vertical. Using small-amplitude analysis they found that maximum meridional particle excursion coincided with the depth of maximum meridional two-particle dispersion that occurs at the critical level. Here, we add to this study by considering a basic state that also varies in the horizontal and has a finite Rossby number. We further investigate mean-flow evolution, both in the small amplitude quasi-linear limit and in the finite amplitude nonlinear regime. Several techniques are used to analyze the flow: a small-amplitude theory for the zonal mean characteristics of floats and tracers, a direct comparison of the small amplitude results to a numerical model run, and finally, the behavior of floats and tracers when the baroclinically unstable waves grow to finite amplitude. Comparison of stirring and mixing in our study highlights the usefulness and limitations of the small-amplitude theory.

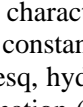
The flow analyzed here consists of two layers of constant density with a basic state that has a meridionally confined jet in the upper layer and a quiescent lower layer. This model shares several features observed in the Gulf Stream such as a near-surface jet, a PV front, and the presence of baroclinic instability. To analyze the float and tracer behavior in this flow we apply the formalism of generalized Lagrangian mean (GLM) theory. This theory provides a framework to analyze and quantify Lagrangian behavior. Using a small amplitude expansion of the governing equations, the theory gives predictions of zonal mean quantities such as the velocity and displacement of the center of gravity of Lagrangian floats. The theory connects these quantities to the underlying wave field through the Stokes drift. The evolution of the zonal-mean tracer distribution is analyzed following the theoretical work of Rhines and coworkers ([Rhines 1977](#); [Rhines and Holland 1979](#)) and [Andrews and McIntyre \[1978, see also McIntyre \(1980\) and a review in Andrews et al. \(1987\), herein AHL\]](#). The evolution of zonal-mean or time-mean quantities is the focus of these approaches and has been used in analytical studies (e.g., [Rhines and Holland 1979](#); [Uyru 1979](#); [Matsuno 1980](#); [Shepherd 1983](#)), as well as in the analysis of numerical model results of baroclinically unstable flows ([Dunkerton et al. 1981](#); [Plumb and Malmann 1987](#)).

The Gulf Stream exhibits neither periodic nor steady spatially growing meanders, two simple cases where the above wave-mean flow interaction theories are directly applicable. However, much of our theoretical understanding of the Gulf Stream is based on such simplified assumptions that capture many of its observed features [e.g., meander growth and propagation speeds ([Killworth et al. 1984](#)) and eddy forcing of the time mean flow ([Cronin 1996](#))].

In [section 2](#), the model and the theoretical background are introduced. We solve for Lagrangian and tracer diagnostics of unstable flows of varied Rossby number in [section 3](#) and discuss their relation to those of stable waves. Numerical model results for a flow with intermediate Rossby number and finite-amplitude meander are presented and contrasted with the small-amplitude theoretical results to evaluate their applicability. In [section 4](#), the large amplitude numerical model results are presented. In [section 5](#), the results are summarized and their applicability to the Gulf Stream is discussed.

2. Model flow and theoretical background

a. Basic state

To evaluate how Lagrangian floats and tracers behave in a baroclinically unstable jet, we use a simple model whose Eulerian characteristics are known (Boss et al. 1996, herein BPT; Boss and Thompson 1999, herein BT). There are two pools of constant PV in the upper layer overlaying a quiescent lower layer (Fig. 1 ). The fluid is assumed to be Boussinesq, hydrostatic, rigid-lid, and on an f plane. We refer to this set of approximations as the shallow water approximation (SW). The zonal geostrophic basic-state (denoted by superscript zero) depth and velocity structure in the upper layer are

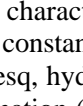
$$h_1^0 = \begin{cases} H_{11} \left[\left(\left(\frac{H_{12}}{H_{11}} \right)^{1/2} - 1 \right) \exp(y/R_{d,1}) + 1 \right] & \text{for } y < 0 \\ H_{12} \left[\left(\left(\frac{H_{11}}{H_{12}} \right)^{1/2} - 1 \right) \exp(-y/R_{d,2}) + 1 \right] & \text{for } y > 0 \end{cases} \quad (1)$$

and

$$u_1^0 = -\frac{g'}{f} \frac{dh_1}{dy} = U_0 \begin{cases} \exp(y/R_{d,1}) & \text{for } y < 0 \\ \exp(-y/R_{d,2}) & \text{for } y > 0, \end{cases} \quad (2)$$

where g' and f are the reduced gravity and the Coriolis parameter and

$$U_0 = (g'H_{11})^{1/2} - (g'H_{12})^{1/2} \quad \text{and} \quad R_{d,j} \equiv (g'H_{1j})^{1/2}/f \quad (3)$$

are the jet maximum speed and the (different) deformation radii on each side of the front. The basic state's potential vorticity is given by $q_{1j}^0 \equiv f/H_{1j}$, where j denotes the side of the PV front (1 being south, $y < 0$) and H_{1j} the fluid depth at $y \rightarrow \mp\infty$ (Fig. 1 ). The flow is confined to within a deformation radius of the potential vorticity front. The lower-layer depth is $h_2^0 = H_T - h_1^0$, where H_T is the total fluid depth, and $u_2^0 = 0$.

In order to study this flow as a function of Rossby number, it is convenient to nondimensionalize the variables by transforming

$$t \rightarrow \frac{tR_d}{U_0}, \quad (x, y) \rightarrow (x, y)R_d, \quad (u, v) \rightarrow (u, v)U_0,$$

$$h_i \rightarrow h_i H_1 \quad \text{and} \quad \psi_i \rightarrow p_i (g'H_1)^{1/2} U_0,$$

where

$$H_1 \equiv (H_{11} + H_{12})/2, \quad R_d \equiv (g'H_1)^{1/2}/f \quad (4)$$

in which H_1 is the y -averaged upper-layer depth and R_d the radius of deformation based on H_1 . The Rossby number, $\epsilon \equiv |U_0|/fR_d$, is a measure of the strength and asymmetry of the initial geostrophic flow (BPT). The flow depends on only the Rossby number ϵ and the depth ratio ($r = H_T/H_1$).

This simple flow exhibits a baroclinic zonal transport and a most unstable wave growth rate that are similar to those observed for the Gulf Stream (see BT for a more detailed comparison). Special cases of this PV-front model have been considered in the past and applied to the Gulf Stream; when $\epsilon = (2)^{1/2}$ ($H_{12} = 0$) the model reduces to the outcropping front

studied by [Killworth et al. \(1984\)](#) and [Wood \(1988\)](#). The QG case is recovered in the limit $\epsilon = 0$ (BPT). The above model in the limit $r \rightarrow \infty$ becomes the $1\frac{1}{2}$ -layer model studied for $\epsilon = (2)^{1/2}$ by [Stommel \(1965\)](#) and [Paldor \(1983\)](#), for variable ϵ by [Williams \(1991\)](#), and for QG by [Pratt and Stern \(1986\)](#) and [Pratt et al. \(1995\)](#). In -BPT and [Boss \(1996\)](#), we summarize the results found in those studies and interpret them in terms of the linearized waves found in the different models. In particular we find that the PV-front model is baroclinically unstable for all values of ϵ and finite r . The vortical (Rossby like) waves taking part in the instability are trapped to the PV gradient near $y = 0$ and are found for all ϵ . They are well approximated by the QG solution. The Eulerian mean evolution of the baroclinic instability is explored at small and large meander amplitude and for various Rossby number flows in BT. At all values of meander amplitude the baroclinic evolution of the QG flow was found to approximate well that of the SW flows.

Here we analyze this model for its tracer and Lagrangian characteristics in both its QG limit (assuming $\epsilon = (2)^{1/2}/2$) and a SW model with the same Rossby number for small amplitude meander. The depth ratio ($r = H_T/H_1$) is taken from the Gulf Stream's parameters in the region east of Cape Hatteras, where the total depth $H_T \sim 4000$ m and the mean thermocline depth $H_1 \sim 500$ m yielding $r \sim 8$.

b. Quasi-linear formulation

To understand the first-order effect of unstable waves on the transport of floats and tracers, we assume that the deviations from the basic-state variables (the waves, denoted by primes) are small relative to the amplitude of the basic state (introduced above and denoted with superscript zero) and have meridionally varying amplitudes and normal mode structure, $\theta = a\text{Re}\{\theta'(y)e^{i(kx-\omega t)}\}$, where θ' denotes any perturbation (wave) variable and a denotes the amplitude of the perturbation. For unstable flows, the frequency ω is complex and its imaginary part, ω_I , is the growth rate. The solution for $\theta'(y)$ is found by linearizing the momentum and continuity equations about the basic zonal-mean flow and solving for the normal modes [[Phillips \(1954\)](#) and, for our flow, BPT].

The modification of zonal mean quantities from the basic state due to the waves [denoted by tilde, (\sim)] is then found by substituting these perturbation solutions into zonally averaged equations [[Phillips \(1954\)](#) and for our flow, BT] where the zonal mean is defined by $\bar{(\)} \equiv \lambda^{-1} \int_0^\lambda (\) dx$, $\lambda \equiv 2\pi/k$. While the normal mode perturbations, $A(y)e^{i\phi}$ and $B(y)e^{i\phi}$, have no zonal mean structure, their correlations can have a zonal mean structure since

$$\overline{\text{Re}\{A(y)e^{i\phi}\}\text{Re}\{B(y)e^{i\phi}\}} = \frac{1}{2}\text{Re}\{A(y)B(y)^*\}e^{2\text{Im}\{\phi\}},$$

where the asterisk denotes the complex conjugate and $\phi = ik(x - \omega t)$. The modifications of mean quantities are thus $O(a^2)$ and are proportional to $e^{2\omega_I t}$. The amplitude expansion of the zonal mean of a variable therefore is $\bar{\theta} = \theta^0(y) + a^2\bar{\theta}(y)e^{2\omega_I t} + O(a^3)$. Notice that with this definition $\bar{\theta}$ is $O(1)$.

Underlying this amplitude expansion is the requirement of small perturbation amplitude, $ae^{\omega_I t} \ll 1$. Also, it is assumed that only a single wave is present in each layer, the one with the highest growth rate of linear baroclinic instability. Using this decomposition, both the first-order Lagrangian mean velocities and the evolution of a passive tracer can be predicted.

c. The generalized Lagrangian mean

Complete Eulerian and Lagrangian descriptions of a flow contain the same information. However, once averaging is performed, some information is lost, and the zonal-mean Eulerian and Lagrangian descriptions contain different information. Here we describe the zonal mean movement of Lagrangian particles using the generalized Lagrangian mean formalism ([Andrews and McIntyre 1978](#)). The GLM theory gives a prediction for the velocity of the center of mass of a line of particles initially parallel to the basic-flow streamlines (which we refer to as the ‘‘centroid’’). For small amplitude waves this velocity is the sum of the Eulerian mean velocity plus the Stokes drift.

Within a layer n ($=1, 2$), the Lagrangian particle displacement \mathbf{X}_n is related to the velocity field \mathbf{u}_n by the kinematic relation $d\mathbf{X}_n/dt = \mathbf{u}_n$. For small amplitude waves, [Andrews and McIntyre \(1978\)](#) defined a mean-free Lagrangian parcel displacement, $\xi'_n \equiv (\xi'_n, \mu'_n, h'_n)$, associated with a normal-mode wave (perturbation) velocity \mathbf{u}'_n , which to $O(a)$ is

$$D_n \mu'_n = \mathbf{v}'_n, \quad (6)$$

$$D_1 h'_1 = -w'_1 - \mathbf{v}'_1 \frac{dh_1^0}{dy}, \quad (7)$$

$$D_2 h'_2 = w'_2 - \mathbf{v}'_1 \frac{dh_2^0}{dy}, \quad (8)$$

where $D_n \equiv ik(u_n^0 - c)$ is the $O(1)$ expansion of the total derivative. [Equations \(7\) and \(8\)](#) are the evolution equations for the interface thickness and could be thought of as the kinematic boundary conditions at the layer's interface, where the vertical perturbation velocity³ is $w'_n = \pm(iku'_n + \mathbf{v}'_{ny})/h_n^0$ from continuity and the fact that in shallow water, the horizontal velocities are uniform within layers. The displacement vector (ξ'_n) is nondivergent [$\nabla \cdot \xi'_n = O(a)$]. Notice that the displacements are nearly singular near critical lines where $u_n^0 - c$ approaches zero.

The GLM velocity \mathbf{u}_n^L for small-amplitude meanders is ([Andrews and McIntyre 1978](#))

$$\begin{aligned} u_n^L &= u_n^0 + \tilde{u}_n + \overline{\xi'_n iku'_n} + \overline{\mu'_n u'_{ny}} + \frac{\overline{\mu_n'^2}}{2} u_{nyy}^0, \\ v_n^L &= \tilde{v}_n + \overline{\xi'_n ikv'_n} + \overline{\mu'_n v'_{ny}}, \\ w_n^L &= \tilde{w}_n + \overline{\xi'_n ikw'_n} + \overline{\mu'_n w'_{ny}} + \frac{h'_n w'_n}{h_n^0}. \end{aligned} \quad (9)$$

Here, $u_n^0 + \tilde{\mathbf{u}}_n$ is the zonal (Eulerian) mean velocity to $O(a^2)$, where u_n^0 is the basic-state flow. In addition, the GLM velocity (minus the basic flow) is proportional to $e^{2\omega t}$; thus it grows in time for unstable waves and is constant for stable waves. For the normal-mode waves studied here (which is proportional to $e^{ik(x-ct)}$), the average of the velocity of particles equally distributed over a line spanning a wavelength (the GLM velocity) is equal to the average of the velocity of a single particle over the wave period (both are averages over the wave phase). The latter is familiar from the theory of surface gravity waves.

The difference between the GLM velocity and the Eulerian mean velocity $\mathbf{u}_n^{\text{SD}} \equiv \mathbf{u}_n^L - \mathbf{u}_n^0 - \tilde{\mathbf{u}}_n$ is the Stokes drift, that is, the difference between the average velocity of a drifting particle relative to the velocity at the average position of that particle. It can arise both from basic-state curvature and/or a spatially varying wave displacement.

There are several differences between meridional Eulerian mean and Lagrangian meridional velocities; the Eulerian zonal-mean (EM) meridional velocity (\tilde{v}_n) and the meridional mass transport ($\mathbf{v}_n \bar{h}_n^-$) are $O(\epsilon)$ because there is no mean zonal pressure gradient (so there is no mean geostrophic meridional flow) and because the vertical displacements (h'_n) are $O(\epsilon)$ compared to the horizontal displacements (BT). The meridional displacement, however, is not constrained by geostrophy ([Uyru 1979](#); [McIntyre 1980](#)) and therefore both the meridional Stokes drift and meridional GLM velocity are $O(1)$ in Rossby number. The Stokes drift is nondivergent ($\nabla \cdot \mathbf{u}_n^{\text{SD}} = 0$) for stable flows and often is divergent for unstable flows ([McIntyre 1980](#)). In contrast, the mean meridional mass transport $\bar{h}_n^- \mathbf{v}_n$ is always nondivergent.

d. Zonal mean tracer evolution

The zonal mean evolution of a passive tracer is governed by the tracer conservation equation $D\chi_n/Dt = 0$. The zonal mean tracer concentration to second order in amplitude is given by $\bar{\chi}_n = \chi_n^0(y) + a^2 \bar{\chi}_n^{\text{SD}}(y) e^{2\omega t}$, with the second term arising from

the presence of an $O(a)$ tracer perturbation, $\text{Re}\{a\chi'_n(y)e^{ik(x-\omega t)}\}$. To $O(a)$ the tracer conservation equation (after division by $e^{i(kx-\omega t)}$) is given by

$$D_n \chi'_n = ik(u_n^0 - c)\chi'_n + \mathbf{v}'_n \chi^0_{ny} = 0. \quad (10)$$

Together with (6) it can be rewritten as

$$D_n(\chi'_n + \mu'_n \chi^0_{ny}) = 0. \quad (11)$$

This implies that, if the perturbation of the tracer is initially zero [i.e., the tracer is zonally uniform (Rhines and Holland 1979)], then

$$\chi'_n = -\mu'_n \chi^0_{ny}, \quad (12)$$

which links the tracer perturbation with the zonal-mean tracer distribution.

The mean tracer modification $\tilde{\chi}_n(y)$ arises from the presence of waves and is found from the $O(a^2)$ expansion of the zonally averaged tracer conservation equation:

$$\overline{D\chi_n/Dt} = e^{2\omega t}(2\omega_I \tilde{\chi}_n + \tilde{\mathbf{v}} \chi^0_{ny} + \overline{\mathbf{v}'_n \chi'_{ny}} + \overline{u'_n ik \chi'_n}) = 0. \quad (13)$$

Substituting (12) in (13) and recasting (13) as an advection diffusion equation gives

$$\tilde{\chi}_{nt} + \mathbf{v}^T \chi^0_{ny} = (\overline{\tilde{\mu}'_n \tilde{\mathbf{v}}^T \chi^0_{ny}})_y \equiv (\kappa^{yy}_n \chi^0_{ny})_y, \quad (14)$$

where

$$\begin{aligned} \mathbf{v}_1^T &\equiv \tilde{\mathbf{v}}_1 + \overline{w'_1 \mu'_1 / h_1}, \\ \mathbf{v}_2^T &\equiv \tilde{\mathbf{v}}_2 - \overline{w'_2 \mu'_2 / h_2}, \quad \text{and} \quad \kappa_n^{yy} \equiv \overline{\mu'_n \mathbf{v}'_n} = \omega_I \overline{\mu_n'^2}, \end{aligned} \quad (15)$$

are the tracer transport velocities in each layer, and κ^{yy}_n is the Lagrangian diffusivity (Rhines and Holland 1979). Here κ^{yy}_n is proportional to the cross-stream two-particle dispersion $\mu_n'^2$ with the growth rate as the proportionality constant (AHL). Both are nonzero only for transient waves and are strictly positive for growing unstable waves.

Similar to the EM meridional velocity, \mathbf{v}^T_n is $O(\epsilon)$. Here κ^{yy}_n is $O(1)$ and is spatially inhomogeneous in a divergent Stokes drift field [such as for an unstable flow, Plumb and Mahlman (1987)]. Thus the dominant balance in (14) for small Rossby number flows is between the time rate of change of the tracer perturbation and the eddy diffusion term.

Another interesting result is derived by multiplying (12) by \mathbf{v}'_n and zonally averaging:

$$\mathbf{v}'_n \overline{\chi'_n} = -\kappa^{yy}_n \chi^0_{ny}. \quad (16)$$

This implies that for a growing (unstable) wave the meridional “eddy” flux of tracer (as well as PV) is down the mean tracer gradient (Rhines and Holland 1979). Substituting q for χ , (16) shows a fundamental difference between stable and unstable waves. Unstable waves flux PV across mean PV contours, whereas stable waves do not (Rhines and Holland 1979; Lozier and Bercovici 1992).

For the physical situation that we study below in the small amplitude limit, the Lagrangian diffusivity (two-particle dispersion) is indicative of stirring that occurs only within a layer (along isopycnals) and is due to eddy processes since the model is inviscid. In the numerical model, small momentum and tracer diffusivities may cause irreversible mixing, but once again only along isopycnals. When the flow is linear, steady and adiabatic (under *nonacceleration* conditions, AHL), the

tracer transport velocity is equal to the mass transport velocity ($\mathbf{v}_n \bar{h}_n / h_n^0$). In general and in our model, both vanish for such stable (linear) waves, and no net meridional transport occurs (this result is referred to as the *nontransport* theorem, AHL).

Mixing requires both stretching and folding (e.g., [Ottino 1989](#)). The Lagrangian diffusivity is indicative of stretching but not of folding, which requires rotation. As a measure of rotation (vorticity) we use another diffusion-like term proportional to the cross-correlation of the zonal and meridional displacement:

$$\kappa_n^{xy} = \overline{\mu_n^x \mu_n^y} = \omega_n \overline{\mu_n^x \xi_n^y}.$$

While this term does not appear in the zonal-mean Lagrangian and tracer equations (due to zonal averaging, although it does appear in the time mean equations), we will demonstrate below that it is an important term to use to infer mixing from stirring. In QG κ_n^{xy} equals half the angular momentum of the waves ([Rhines and Holland 1979](#)). When time mean equations are derived, κ_n^{xy} appears in the off-diagonal terms of the diffusivity tensor ([Rhines and Holland 1979](#)).

Several connections can be made between the mean tracer formulation and the GLM. First, the Lagrangian velocity is the velocity of the center of mass of a patch of tracer ([Plumb and Mahlman 1987](#)). In addition (e.g., AHL),

$$\mathbf{v}_n^L = \mathbf{v}_n^T + \kappa_n^{yy} \mathbf{e}_y, \quad (17)$$

which for a small Rossby number flow (17) implies that $\mathbf{v}_n^L \sim \mathbf{v}_n^{\text{SD}} \sim \kappa_n^{yy} \mathbf{e}_y$; that is, the Lagrangian velocity is dominated by the Stokes drift, which is approximated by the gradient of the Lagrangian diffusivity.

e. Solution method

In this section we outline the procedure for computing the Stokes drift, the Lagrangian and tracer velocities, and the Lagrangian diffusivity. For the analytical quasi-linear calculations we use the most unstable wave solutions derived in BPT to compute the Stokes drift. Summing it with the Eulerian mean velocities (solved in BT) provides the Lagrangian velocities (9). Similarly the tracer velocity and diffusivity are computed using (15).

For the numerical model (the appendix), we compute the Lagrangian velocity from its definition, the *ensemble averaged* velocity of particles initially equally spaced and aligned parallel to the jet axis. The time rate of change of the zonal-mean tracer distribution is calculated from its definition, χ_{nt} .

To facilitate comparison of numerical results and theory, all quantities are normalized by the square perturbation amplitude a^2 , where $a = [2\mu'_1(y=0)]/\lambda$ is the ratio of the maximum horizontal displacement of the front $[\mu'_1(y=0)]$ to half the (dimensional) meander wavelength λ . The horizontal displacement of the front (dimensional) will be given by $a\lambda/2$ and since the most unstable wave in our model has a typical length of $10.5R_d$, $\mu'_1(y=0) = a \cdot 5.25R_d$. We compute the quasi-linear GLM and mean tracer variables for two different flows: a QG flow with $\epsilon = (2)^{1/2}/2$ (with most unstable wavenumber $k = 0.58$) and a SW flow with the same ϵ ($k = 0.6$).

3. Small amplitude results

a. Application of the theory to the PV-front model

To develop some intuition about the Stokes drift and GLM velocities in the unstable flow, we first analyze the GLM velocities of stable waves (e.g., [Matsuno 1980](#)). In BPT we found that analyzing an instability as a resonance between stable waves, one from each layer, provides physical insight into the instability. Structure and phase of the unstable wave were found to be very similar to those of the resonating stable waves computed in two models, each with one layer identical to the two-layer model plus a second infinite layer (equivalent barotropic or 1½-layer models, [Fig. 2](#) ☞). Here, the same decomposition is used to understand the connection between wave displacements and the Stokes drift for the frontally trapped waves.

The wave trajectories relative to the mean flow and the displacement ellipses ([Fig. 3](#) ☞) display clearly how a Stokes drift comes about. As the particle moves meridionally, the zonal wave displacement changes. Averaged over the phase of the wave, the zonal drift is in the same direction as the particle zonal velocity in the latitude where the zonal displacement is largest. For example, in the lower layer for $y < -2$, the ellipses are cyclonic (clockwise) and the amplitude of the zonal

displacement increases with y resulting in a positive zonal drift. For the upper-layer model there is also a drift due to the mean flow curvature, $\frac{1}{2}\mu_1^{-2}u_1^0$ (9) which is everywhere positive for the model's jet, yet about 20 times smaller in magnitude than the wave-wave terms.

The meridional structure of the zonal Stokes drift of the unstable mode of the two-layer flow is similar in structure and magnitude to that of the stable mode in the two 1½-layer models (compare left and center panels of Fig. 4). Differences are found in the upper layer in the vicinity of the critical lines, where the stable wave Stokes drifts are singular [where $D_n = ik(u_1^0 - c) = 0$]. Also, while the amplitude of the Stokes drifts of stable waves is constant in time, it grows like $e^{2\omega t}$ for unstable waves. The amplitude of the zonal Stokes drift is substantial; a perturbation with $a \equiv 2\mu_1'(0)/\lambda \approx 0.2$ results in a 20% difference between the Eulerian and Lagrangian mean velocities.

No meridional Stokes drift is present for stable waves with meridionally varying amplitudes ($\mathbf{v}_{ny}^{\text{SD}} = 0$; this is similar to the absence of vertical drift of surface gravity waves). The pattern of meridional displacement resulting from stable waves, however, is indicative of the direction of meridional Stokes drift of the unstable waves. Since the maximum meridional displacement occur at the critical lines in the upper-layer model and near $y = 0$ in the lower layer (Fig. 3), where the perturbation amplitude is maximum (Fig. 6 in BPT), we expect the drift to the critical lines (Fig. 3). Indeed, the structure of the meridional Stokes drift of unstable waves (Fig. 4) is consistent with the insight derived from the structure of the stable waves.

The QG solution for the Stokes drift is found to compare well with the SW one except for a discontinuity in the zonal Stokes drift at $y = 0$ in the SW model owing to the discontinuity of u_{1yy}^0 there. The loss of symmetry around $y = 0$ in the SW model arises as a result of the loss of symmetry of the basic-state flow as the Rossby number is increased. In the lower layer the agreement is better than in the upper layer, due to the smaller relative layer depth change across the front.

The GLM meridional velocity ($\mathbf{v}_n^L = \bar{\mathbf{v}}_n + \mathbf{v}_n^{\text{SD}}$) and Lagrangian zonal acceleration⁴ are dominated by the Stokes drift in most of the domain except close to the upper-layer jet, where the EM and Stokes drift are of similar magnitude (Fig. 5 and Fig. 3 in BT). The GLM meridional velocity in the upper layer converges toward the critical lines, being dominated by the Stokes drift. Divergence of the GLM meridional velocity occurs near the jet's center in the upper layer. Although difficult to see in Fig. 5, in the lower layer there is a convergence below the jet whose center shifts south with ϵ .

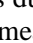

The zonal mean tracer velocity (15) is in the same direction as the zonal mean meridional mass flux (Fig. 6; Fig. 3 in BT), in the direction that reduces the potential energy of the mean flow. Unlike the mass flux, it is divergent and is unequal and opposite in the layers. The upper-layer Lagrangian diffusivity (κ_{11}^{yy} , Fig. 6) is maximum near the critical lines in the upper layer, being proportional to $|u^0 - c|^{-2}$ [(6), (15)]. A similar result was found in a critical level by Lozier and Bercovici (1992). In the lower layer the diffusivity is maximum where the perturbation amplitude is maximum. The maximum is under the jet axis in QG and migrates south with increasing ϵ .

Unlike the meridional diffusivity (κ_n^{yy}) that is of the same magnitude in both layers, κ_n^{xy} is two orders of magnitude larger in the upper layer (with largest value near the critical lines) than in the lower layer. Since both stretching (κ_n^{yy}) and rotation (κ_n^{xy}) are needed for mixing to take place, mixing is predicted to be significantly stronger in the upper layer, as will be seen with the numerical model in the next section. For cyclonic (anticyclonic) rotation, κ_n^{xy} is negative (positive) and is of different sign at the two critical lines (Fig. 6). Stirring (as indicated by the amplitude of both κ_{11}^{xy} and κ_{11}^{yy}) is significantly more intense in the northern critical line in the SW model. This is an ageostrophic effect associated with an increase in the horizontal displacements amplitude on the northern (shallow) side of the front. By continuity, for a given perturbation in layer depth, the associated horizontal response will be larger on the shallower side.

b. Numerical model result with a small-amplitude meander

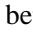
In this section we compare the inviscid quasi-linear results against results from a viscous numerical model with small (but finite) meander amplitude. We use a *free surface* isopycnal model developed by Hallberg (1995), which we initialize with the basic flow corresponding to $\epsilon = (2)^{1/2}/2$. Details on the numerical procedures are found in the appendix.

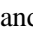
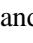
The GLM meridional velocities computed from the model floats agree quantitatively well with the theoretical prediction

(Fig. 7 ). The largest difference is due to the difference in location of the critical lines in the numerical model due to the inevitable (yet small) differences in mean flow between a free surface and a rigid-lid model. The numerical grid is such that the maximum jet velocity in the model occurs half a grid point relative to the jet center ($0.12R_d$), and thus the biggest differences in u occur for the float released there. In addition, the presence of diffusion (numerical and explicit) affects both the mean flow and the instability growth rate, and thus the position of the critical lines. Agreement between the theoretical prediction with the modeled GLM zonal acceleration is not as good as for the meridional velocities, especially close to the critical lines in the upper layer, which at finite amplitudes develop into a recirculation region with finite meridional extent (see below). Changing our interpolation scheme (from bilinear to nonlinear) and increasing the number of grid points (from 128^2 to 200^2) did not change the results significantly. Lack of quantitative agreement in the upper-layer zonal GLM accelerations is due to existence of a strong $O(1)$ sheared zonal mean flow there. Viscous processes (neither included in our theoretical analysis nor in the way we compute the Lagrangian acceleration with the model results) are acting on the zonal mean jet and are affecting the $O(a^2)$ zonal acceleration because u^0_{1yy} has a discontinuity at the front in the initial condition. The smaller value of the acceleration in both layers is caused by both reduction in the growth rate due to viscosity and nonlinearities as the perturbation grows (Pedlosky 1987) and the smearing of the signal when averaged over a meandering jet. The presence of an Eulerian barotropic mean flow in the model was discussed in BT. Here it causes the zonal GLM velocity to be nonzero at large y . Because there is no $O(1)$ zonal-mean meridional velocity and because it is small close to the jet center where the meander amplitude is greatest, such a contamination of the $O(a^2)$ by the $O(1)$ dynamics is not observed in the meridional-mean Lagrangian velocities (Fig. 7 ).

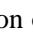
A basic-state tracer field with a linear gradient was chosen to minimize numerical diffusion, and is given by

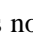
$$\chi_n(t = 0) = \overline{\chi(t = 0)}_n = \bar{\chi}_n(y = 0) + y\bar{\chi}_{ny}. \quad (18)$$

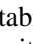
With $\bar{\chi}_n(y = 0) = 0.5$ and $\bar{\chi}_{ny} = (-1)^n 0.032$, the concentration varies from 0 to 1 over the model domain and is in opposite directions in each layer. The numerical results of $\bar{\chi}_{nt}/\bar{\chi}_{ny}$ are in good quantitative agreement with the quasi-linear calculations of $\bar{\chi}_{nt}/\bar{\chi}_{ny}^0$ (Fig. 8 ). Differences between model and theory are biggest near the southern critical line.

For our choice of mean tracer field $\chi_n^0, \kappa^{yy}_n \chi_{ny}^0 \approx \mathbf{v}^{\text{SD}}_n \chi_{ny}^0$ (17) is the forcing on the rhs of (14), which explains the similarity between \mathbf{v}^L_n in Fig. 7  and $\bar{\chi}_{nt}/\bar{\chi}_{ny} = \kappa^{yy}_n - \mathbf{v}^T_n$ in Fig. 8 . Results of a run with an explicit tracer diffusivity $\kappa = 10 \text{ m}^2 \text{ s}^{-1}$ were quantitatively similar.

4. Large-amplitude numerical model results

While the small-amplitude theory is useful where it is applicable, for meander amplitudes on the order of a wavelength no similar theory is available. Here we investigate the finite amplitude Lagrangian and tracer evolution and inquire, in particular, whether the features which have their seeds in the small-amplitude theory appear when the meanders reach finite amplitude. The energetics evolution as a function of time (bottom of Fig. 9 ) is used to trace the instability evolution from its linear phase where the perturbation energy grows exponentially to the equilibration phase over which the long-term energetic growth is algebraic.

As predicted from the small-amplitude theory, the float centroids initially converge toward the critical lines in the upper layer and slightly south of $y = 0$ in the lower layer due to migration of the maximum in perturbation amplitude southward (BPT, BT). In the upper layer, with time, the float centroids continue to drift past the positions where critical lines were initially found (Fig. 9 ). This does not indicate a change in the float response to mean-flow characteristics, but rather is due to the migration of the critical lines toward $y = 0$ as the mean flow weakens (the phase speed also weakens but, apparently, slower). Also, for finite amplitude waves, critical lines bifurcate, creating recirculation regions. For stable waves the meridional extent of the recirculation regions was found to be proportional to the square root of the amplitude and inversely proportional to the mean flow shear (Pratt et al. 1995). Zonal averaging over these evolving regions is also responsible for the observed migration. Beyond equilibration (at about $t \sim 200$) the convergence pattern is more erratic, especially on the northern side, and multiple zonal jets are present (BT). In the lower layer, convergence toward the front continues beyond $t \approx 200$. As the lower layer jet is accelerated, the centroids spread into two main convergence zones ($t \sim 250$).

Centroids intersect prior to the instability equilibration (Fig. 9 ) , at which time the functional mapping from the initial position of the centroid to its final position is nonunique. Since Lagrangian means are meaningful only relative to the parcel initialization, a reinitialization procedure may be warranted at such a time (McIntyre 1980; Dunkerton et al. 1981). However, it is interesting that even long after the centroid positions cross, the meridional Lagrangian velocity is in the same direction as

predicted by the small-amplitude theory.

By the end of the simulation ($t \sim 375$), the spread of the centroids is approximately equal in both layers with slightly more centroids north of $y = 0$ than south in both layers. In the upper layer this pattern is consistent with the increase in Lagrangian diffusivity to the north (Fig. 6). In the lower layer a similar pattern of Lagrangian diffusivity is expected once a substantial mean jet has accelerated there (BT).

We emphasize that *individual* floats in the upper layer do not cross the local position of the PV front prior to eddy detachment at $t \sim 290$. Individual floats and *centroids* of lines of floats cross the *mean* position of the front and jet (Fig. 9). Individual lower-layer floats do cross below the local position of the upper-layer PV front since the lower-layer perturbation is phase lagged relative to the upper layer's meander. This phase lag is characteristic of baroclinic instability.

Coincident with the float centroid convergence to the critical lines with increased meander amplitudes is the formation of recirculation regions around the location of the critical lines. The recirculation regions are clearly seen in the tracer distribution field (Fig. 10). Two phenomena, pooling and recirculation, govern the tracer distribution. Pooling refers to the process of convergence/divergence of fluid due to differential advection, and recirculation refers to the process whereby fluid parcels are folded against each other and requires the presence of vorticity. Since the perturbation amplitude decays meridionally away from the jet core, fluid is pooled between successive troughs and crests of the meander near the front, with increases of tracer gradients away from the front in both layers (Fig. 10). Recirculation in the pools in the upper layer causes mixing through shear dispersion, with increased gradients on the edges of the recirculation regions, especially on the side facing the jet core. Pooling with no recirculation occurs in the lower layer, resulting in a very different tracer field evolution. Pooling occurs where the eddy diffusivity of the quasi-linear theory is maximum (Fig. 6), while recirculation occurs where the displacement cross-correlation is maximum. Note that the recirculation direction is the same as predicted by the sign of κ^{xy}_n and that it is intensified on the northern side, as predicted by the previous section's results.

The structure of the zonal-mean meridional tracer gradients $\bar{\chi}_y$ is similar in both layers, yet it is an order of magnitude stronger in the upper layer at $t \sim 188$ (Fig. 10); the gradient is weak near the mean front position and strong on the edges of the meander, particularly on the northern side. This pattern is consistent with the Lagrangian diffusivity structure in the lower layer (Fig. 6). In the upper layer one may expect a gradient maximum at the front (there exists a minimum in eddy diffusion there, Fig. 6). Indeed, for small amplitude (not shown) the upper-layer mean tracer gradient matches that predicted from Fig. 6, with two regions of minimum gradients on either side of the front. However, as the amplitude of the meander increases, the recirculation regions overlap in their meridional position (although at different zonal locations), resulting in $t \sim 188$ in the observed zonal mean tracer gradient. In the upper layer, the tracer is entrained into the growing recirculation regions where enhanced mixing takes place. As the growth of the recirculation regions slows and during eddy detachment, mixing within the recirculation regions resembles mixing within closed streamlines; the tracer homogenizes within recirculation regions and results in the migration of the tracer gradient toward the edges of these regions, the jet axis on one side and the far field on the other side.

In order to quantify tracer mixing, as opposed to stirring, we conducted experiments with varying explicit tracer diffusivities: $\kappa = 0, 10, 100, \text{ and } 1000 \text{ m}^2 \text{ s}^{-1}$ and respective Peclet numbers $\text{Pe} = U_0 R_d / \kappa = \infty, 6000, 600, \text{ and } 60$. The momentum field and initial basic tracer field were the same for all the runs. We quantified the mixing by binning both the PV and tracer concentrations at each model grid point into six different bins. Assuming θ is either tracer concentration or PV, the bin boundaries are $\min(\theta) + (0, 0.1, 0.3, 0.5, 0.7, 0.9, 1.0) \cdot [\max(\theta) - \min(\theta)]$. At each time step we compute the fluid mass within each bin (i.e., tracer mass). The conversion of fluid from one bin to another can only occur if mixing is present and represents the *net* amount of fluid converted and is a lower bound to the actual volume of water changing its tracer value. This analysis is similar to Nakamura's (1996) formulation of tracer mixing in area coordinates.

Tracer mass conversion intensifies at $t = 200$, about when the primary instability equilibrates, and continues at a rapid rate (almost exponentially) until $t = 290$ when eddy detachment occurs (Fig. 11). The tracer is observed to mix sooner in the upper layer due to the presence of the recirculation regions. For PV, less mixing occurs initially in the upper layer than in the lower layer since initially there is no PV gradient in the vicinity of the critical lines in the upper layer (the only PV gradient is at the front). Until $t \sim 290$ mixing is weakly dependent on Pe, except for the bins of concentration adjacent to the wall (where a no flux condition is applied, forcing the tracer values to change). After $t > 290$ mixing is Pe dependent.

5. Discussion and conclusions

We conducted a quantitative comparison of the Lagrangian mean and zonal-mean tracer-related quantities derived from theory of inviscid flows with results from a numerical model. For small-amplitude meanders we find good quantitative agreement between theory and numerical model results. The Lagrangian zonal acceleration did not compare as well near the jet center. We believe this is due to contamination of the mean by modification owing to viscous effects on the jet, which are not included in the theory.

Comparison of QG and SW reveals that the QG model does well in predicting the magnitude and direction of Lagrangian and tracer quantities. Differences in the results arise from the differences in the basic state between the two cases. This result is consistent with BT's result that the baroclinic evolution of the front is weakly dependent on the Rossby number.

Both the tracer and Lagrangian analysis support the following mixing scenario for a baroclinically unstable jet: in the initial phase of the instability, recirculation regions located at the critical lines in the upper layer, grow exponentially, and entrain new fluid. At this stage, in the upper layer, there is little dependence of mixing on Peclet number (Fig. 11). As the baroclinic instability equilibrates, fluid is found to mix vigorously within the recirculation regions with continuous (yet slower) entrainment of new fluid into these regions. Mixing causes tracer gradients to migrate toward the edge of the recirculation regions and a strong property gradient is maintained at the meandering jet and at the outer edge of the recirculation regions. The zonal mean gradients, however, are reduced when the recirculation regions from both sides of the jet meridionally overlap (and yet they continue to be zonally separated, Fig. 10). The recirculation regions continue to grow algebraically until barotropic shear destroys the coherent flow; eddies detach, and a cascade of secondary instabilities ensues (BT). After eddy detachment occurs, mixing is found to depend more strongly on the value of the Peclet number (Fig. 11).

In the lower layer there are initially no recirculation regions and consequently very little mixing occurs. Intense lower-layer mixing does not take place until after the lower-layer jet accelerates.

Until eddy detachment, the mixing pattern is consistent with that predicted from two eddy diffusivity terms. At the critical lines, where κ_n^{yy} and κ_n^{xy} are present, there is stretching and folding causing enhanced mixing, which is weakly dependent on the value of the tracer diffusivity. Where only stretching is present, as in the lower layer, mixing is significantly smaller.

Shepherd (1983) found that QG models with different basic states were similar in their Eulerian structure, yet quite different (in direction and magnitude) in their GLM velocity and attributed the difference to the changes in the structure of the basic-state shear. Similarly we find that changes in the shear between the basic states of QG and SW result in a bigger difference between the mean Lagrangian velocities of the two models than between the Eulerian mean velocities (compare Fig. 4 here with Fig. 2 in BT).

As the instability equilibrates and growth becomes algebraic, the fluid within the recirculation regions mixes in a process similar to, but faster than, tracer homogenization within closed streamlines, which was found to be initially proportional to $Pe^{2/3}$ (Rhines and Young 1983). When the recirculation regions detach to form eddies, the theory of tracer homogenization within closed streamlines should apply within them, and indeed, we notice a dependence of the mixing rate on the Peclet number (Fig. 11).

Plumb and Mahlman (1987) found the zonally averaged eddy diffusivity tensor to be a good predictor for the rate of mixing observed in most regions of a three-dimensional atmospheric GCM. As in our case, their diffusivity tensor does not include the term κ^{xy} . The disagreement, we believe, stems from the flows under study. While we analyze the tracer evolution in a free, localized unstable flow, Plumb and Mahlman (1987) analyzed tracer evolution in an equilibrated, forced dissipative system.

The PV structure of our model is such that there are no dynamical critical lines. The PV equation is regular at the upper layer's critical lines because the PV there has no gradient. Inclusion of such a gradient may affect the results since additional unstable modes may be present. However, studies of similar baroclinic jets on a β plane suggest that the dynamics are similar (Ikeda 1981; Wood 1988). Also, if a gradient in PV occurred there, one would expect it to be reduced by the same processes that cause the tracer to mix due, possibly, to breaking of modes associated with critical lines. The kinematics of tracers and Lagrangian particles are therefore not expected to change qualitatively but possibly quantitatively. While it has been shown that, for a neutral wave to exist, a critical line must coincide with a region of constant PV, unstable waves can have critical lines in regions of PV gradient (Lozier and Bercovici 1992; Pratt et al. 1995).

Despite differences in their dynamics, we find similarities between a snapshot of tracer distribution prior to eddy detachment in our model (Fig. 10) and tracer distributions in barotropic and equivalent barotropic jet models that are either stable or equilibrated (e.g., Rogerson et al. 1996, manuscript submitted to *J. Phys. Oceanogr.*). In all cases finite-amplitude waves create recirculation regions around which the critical lines lie and within which the tracer recirculates. In order for mixing to occur within stable barotropic and equivalent barotropic jets, a second wave is needed that causes a recirculation region to exchange fluid with its surroundings. In our case, temporal growth of the unstable mode supplies the recirculation regions with new fluid. Mixing within the recirculation regions in all models will depend, among other factors, on the tracer diffusivity and on the rate of supply of new fluid into the recirculation regions.

For a single stable wave the meridional Stokes drift vanishes. As one reviewer remarked, when more than one wave is

present, correlations between the waves may result in a Stokes drift. However, since the waves have different phase speed, two critical lines will exist, changing the geometry of the problem. Still, it is conceivable that GLM theory may be generalized to cases where stirring occurs when more than one stable wave is present. It would be interesting to see how predictions of such a calculation compare with those derived from the theory of dynamical systems.

The theory and the model both point at the different structure of the Lagrangian mean and Eulerian mean jet. We find the GLM zonal velocity to be faster than the Eulerian mean zonal velocity on the north side of the front and slower on the south side (Fig. 5), $u_{mt}^L \propto u_n^L - u_n^0$ for an intermediate $O(1)$ Rossby number jet. While such an analysis has not been attempted with Gulf Stream floats, there is an indication that downstream velocity averaged over floats differs from Eulerian measurements, even though the overall structure of the jet in streamline coordinates changes slowly downstream of Cape Hatteras. For instance, a suggestion of the difference between Eulerian and Lagrangian structure of the stream may be found in the analysis by Song et al. (1995), who calculated the downstream float velocities of 64 RAFOS floats adjacent to the 14.5° isotherm. Downstream velocity maps averaged over floats present in either meander crests or troughs (their Fig. 10) show an inflection point in the downstream on the anticyclonic shear side of the jet (north), which was more pronounced for floats at crests. Although this average over floats is not the same as the averaging used in GLM, it is based on float velocities, as opposed to Eulerian measurements. Eulerian velocity measurements of the downstream velocity above the 12°C isotherm in the Gulf Stream [e.g., Fig. 9 of Johns et al. (1995)] suggest that the shear of the downstream current on either side of the jet maximum is single signed along both isotherms and isobars. Here we suggest that the difference between the mean Lagrangian and Eulerian observations of the Gulf Stream is due to the inherent differences between them, as formulated by the Stokes drift in the small-amplitude theory.

We find convergence of the centers of gravity of floats to the critical lines (where the displacement are maximum) in the upper layer and to the location of the maximum in displacement in the lower layer. Freeland et al. (1975) observed a migration of the centers of gravity of floats toward areas of higher displacement (as quantified by increased eddy kinetic energy) in the MODE region.

Analysis of float trajectories, released within the Gulf Stream, inferred that the PV front (Bower and Lozier 1994) or the jet axis (Song et al. 1995) provided a barrier to float crossing. The two sites cannot be distinguished with the available data (A. S. Bower 1997, personal communication). While in our model no individual Lagrangian parcels crossed the PV front prior to eddy detachment, we find that, averaged over lines of floats, it is the location of the minimum in eddy diffusivity (slightly south of the PV front in our SW model's upper layer) that separates centroids migrating north and south to the maxima in diffusivity at the critical lines. The role of the critical lines as the location where enhanced stirring takes place and where fluid and Lagrangian particles are entrained seems robust in observations (Lozier et al. 1997) as well as in previous theoretical work. Besides being sites of enhanced two-particle dispersion these regions exhibit vorticity, necessary for mixing.

The role of the critical surface in the distribution of tracers in the vicinity of the Gulf Stream is suggested by the distribution of O_2 ; strong gradients are observed at the surface close to the PV front while weaker gradients are found on both sides of the stream. At depth ($27.8 > \sigma_\theta > 27.0$), both the PV and O_2 fronts are weaker (Bower et al. 1985). This distribution is consistent with the presence of a critical (or steering) surface within the jet where one would expect enhanced stirring (Bower 1991; Pratt et al. 1995). On the north side of the stream the location of such a surface may be nearly parallel to isopycnals; on the south side this surface is expected to be close to being normal to the isopycnals, potentially contributing to enhanced diapycnal mixing. The oxygen and PV sections of Bower et al. (1985) indeed display a more homogeneous distribution on the southern side. However, surface effects, such as deep winter mixing on the south side of the stream, may confound this hypothesis. The strong property front within the stream is consistent with mixing occurring at the critical lines on both sides, "expelling" the tracer gradient to the vicinity of the jet's axis.

There are several ways in which the dynamical framework used here could be applied to analyze float data in the vicinity of jets. First, all the components of the diffusivity tensor could be computed in the framework of a jet to establish the stirring geometry [Freeland et al. (1975) computed the diagonal terms of the diffusivity tensor from float data collected in the mode region]. Extending the analysis to spatially growing waves, using temporal rather than spatial averaging [e.g., Cronin (1996) for the Eulerian mean], may be of more applicability to the Gulf Stream. For instance, analysis of floats released at a single location relative to the stream, but on different phases of the meander, may be used to compute the Stokes drift.

The simple model introduced here lacks topography, the β effect, continuous stratification, wind convergence, and spatially growing dynamics (as opposed to a reentrant channel), all of which may modify our results with regard to a specific application such as the Gulf Stream. However, the model's simplicity provides increased dynamical insight into the processes that affect geophysical flows and floats and tracers within them.

Acknowledgments

We would like to acknowledge the useful discussions with M. Kawase, K. K. Tung, P. B. Rhines, and D. Swift. Assistance in running and debugging the numerical model was kindly provided by D. Darr. Editorial comments by L. Landrum, D. LeBel, F. Straneo, A. Weiss, and comments from two anonymous reviewer greatly improved this manuscript. E. B. is supported by a National Science Foundation Young Investigator Award to L. T., and L. T. is supported by an Office of Naval Research Young Investigator Award.

REFERENCES

- Andrews, D. G., and M. E. McIntyre, 1978: An exact theory of nonlinear waves on a Lagrangian-mean flow. *J. Fluid Mech.*, **89**, 609–646..
- , J. R. Holton, and C. B. Leovy, 1987: *Middle Atmosphere Dynamics*. Academic Press, 489 pp..
- Boss, E., 1996: Dynamics of potential vorticity fronts. Ph.D. thesis, University of Washington, 168 pp..
- , and L. Thompson, 1999: Mean flow evolution of a baroclinically unstable potential vorticity front. *J. Phys. Oceanogr.*, **29**, 273–287.. [Find this article online](#)
- , N. Paldor, and L. Thompson, 1996: Stability of a potential vorticity front: from quasigeostrophy to shallow water. *J. Fluid Mech.*, **315**, 65–84..
- Bower, A. S., 1991: A simple kinematic mechanism for mixing fluid parcels across a meandering jet. *J. Phys. Oceanogr.*, **21**, 173–180.. [Find this article online](#)
- , and H. T. Rossby, 1989: Evidence of cross-frontal exchange processes in the Gulf Stream based on isopycnal RAFOS float data. *J. Phys. Oceanogr.*, **19**, 1177–1190.. [Find this article online](#)
- , and M. S. Lozier, 1994: A closer look at particle exchange in the Gulf Stream. *J. Phys. Oceanogr.*, **24**, 1399–1418.. [Find this article online](#)
- , H. T. Rossby, and J. L. Lillibridge, 1985: The Gulf Stream—Barrier or blender? *J. Phys. Oceanogr.*, **15**, 24–32.. [Find this article online](#)
- Cronin, M., 1996: Eddy–mean flow interaction in the Gulf Stream at 68°W. Part II: Eddy forcing on the time-mean flow. *J. Phys. Oceanogr.*, **26**, 2132–2151.. [Find this article online](#)
- del-Castillo-Negrete, D., and P. J. Morisson, 1993: Chaotic transport by Rossby waves in shear flow. *Phys. Fluids A*, **5**, 948–965..
- Dunkerton, T. J., C.-P. F. Hsu, and M. E. McIntyre, 1981: Some Eulerian and Lagrangian diagnostics for a model of stratospheric warming. *J. Atmos. Sci.*, **38**, 819–843..
- Easter, R. C., 1993: Two modified versions of Bott’s positive-definite numerical advection scheme. *Mon. Wea. Rev.*, **121**, 297–304.. [Find this article online](#)
- Freeland, H. J., P. B. Rhines, and H. T. Rossby, 1975: Statistical observations of the trajectories of neutrally buoyant floats in the north Atlantic. *J. Mar. Res.*, **33**, 383–404..
- Hallberg, R., 1995: Some aspects of the circulation in ocean basins with isopycnals intersecting sloping boundaries. Ph.D. thesis, University of Washington, 244 pp..
- Ikeda, M., 1981: Meanders and detached eddies of a strong eastward-flowing jet using a two-layer quasi-geostrophic model. *J. Phys. Oceanogr.*, **11**, 526–540.. [Find this article online](#)
- Johns, W. E., T. J. Shay, J. M. Bane, and D. R. Watts, 1995: Gulf Stream structure, transport and recirculation near 68°W. *J. Geophys. Res.*, **100**, 817–838..
- Killworth, P. D., N. Paldor, and M. E. Stern, 1984: Wave propagation and growth on a surface front in a two-layer geostrophic current. *J. Mar. Res.*, **42**, 761–785..
- Kim, H. S., and D. R. Watts, 1994: An observational streamfunction in the Gulf Stream. *J. Phys. Oceanogr.*, **24**, 2639–2657.. [Find this article online](#)
- Lozier, M. S., and D. Bercovici, 1992: Particle exchange in an unstable jet. *J. Phys. Oceanogr.*, **22**, 1506–1516.. [Find this article online](#)
- , L. J. Pratt, and A. M. Rogerson, 1997: Exchange geometry revealed by float trajectories in the Gulf Stream. *J. Phys. Oceanogr.*, **27**,

- Matsuno, T., 1980: Lagrangian motion of air parcels in the stratosphere in the presence of planetary waves. *Pure Appl. Geophys.*, **118**, 189–216..
- McIntyre, M. E., 1980: Towards a Lagrangian-mean description of stratospheric circulations and chemical transports. *Philos. Trans. Roy. Soc. London A*, **296**, 129–148..
- Nakamura, N., 1996: Two-dimensional mixing, edge formation and permeability diagnosed in an area coordinate. *J. Atmos. Sci.*, **53**, 1524–1537.. [Find this article online](#)
- Ottino, J. M., 1989: *The Kinematics of Mixing: Stretching, Chaos, and Transport*. Cambridge University Press, 364 pp..
- Owens, W. B., 1984: Synoptic and statistical description of the Gulf Stream and subtropical gyre using SOFAR floats. *J. Phys. Oceanogr.*, **14**, 104–113.. [Find this article online](#)
- Paldor, N., 1983: Linear stability and stable modes of geostrophic fronts. *Geophys. Astrophys. Fluid Dyn.*, **24**, 299–326..
- Pedlosky, J., 1987: *Geophysical Fluid Dynamics*. Springer-Verlag, 710 pp..
- Phillips, N. A., 1954: Energy transformations and meridional circulations associated with simple baroclinic waves in a two-level, quasigeostrophic model. *Tellus*, **6**, 273–286..
- Plumb, R. A., and J. D. Mahlman, 1987: The zonally averaged transport characteristics of the GFDL general circulation/transport model. *J. Atmos. Sci.*, **44**, 298–327.. [Find this article online](#)
- Pratt, L. J., and M. E. Stern, 1986: Dynamics of potential vorticity fronts and eddy detachment. *J. Phys. Oceanogr.*, **16**, 1101–1120.. [Find this article online](#)
- , M. S. Lozier, and N. Beliakova, 1995: Parcel trajectories in quasigeostrophic jets: Neutral modes. *J. Phys. Oceanogr.*, **25**, 1451–1466.. [Find this article online](#)
- Press, W. H., A. Teukolsky, W. T. Vetterling, and B. P. Flannery, 1992: *Numerical Recipes in C*. Cambridge University Press, 963 pp..
- Rhines, P. B., 1977: The dynamics of unsteady currents. *The Sea*, Vol. 6, E. D. Goldberg, Ed., J. Wiley and Sons, 189–318..
- , and W. R. Holland, 1979: A theoretical discussion of eddy-driven mean flows. *Dyn. Atmos. Oceans.*, **3**, 289–325..
- , and W. R. Young, 1983: How rapidly is a passive scalar mixed within a closed streamline? *J. Fluid Mech.*, **133**, 133–145..
- Samelson, R. M., 1992: Fluid exchange across a meandering jet. *J. Phys. Oceanogr.*, **22**, 431–440.. [Find this article online](#)
- Shepherd, T. G., 1983: Mean motions induced by baroclinic instability in a jet. *Geophys. Astrophys. Fluid Dyn.*, **27**, 35–72..
- Song, T., T. Rossby, and E. Carter, 1995: Lagrangian studies of fluid exchange between the Gulf Stream and surrounding waters. *J. Phys. Oceanogr.*, **25**, 46–63.. [Find this article online](#)
- Stommel, H., 1965: *The Gulf Stream*. University of California Press, 248 pp..
- Uyru, M., 1979: Lagrangian mean motion induced by a growing baroclinic wave. *J. Meteor. Soc. Japan*, **57**, 1–20..
- Watts, D. R., K. L. Tracey, J. M. Bane, and T. J. Shay, 1995: Gulf Stream path and thermocline structure near 74°W and 68°W. *J. Geophys. Res.*, **100**, 18 291–18 312..
- Williams, R., 1991: Primitive equation models of Gulf Stream meanders. WHOI Tech. Rep. WHOI-92-16, 272–285..
- Wood, R. A., 1988: Unstable waves on oceanic fronts: Large amplitude behavior and mean flow generation. *J. Phys. Oceanogr.*, **18**, 775–787.. [Find this article online](#)

APPENDIX

6. Numerical Model Parameters

The numerical model used here was developed by [Hallberg \(1995\)](#) and initialized with the basic state of $\bar{\epsilon} = \sqrt{2}/2$. The model grid (128 by 128 grid points) contains three wavelengths of the most (linearly) unstable wave. We use a grid with $\Delta x = \Delta y = 0.247\bar{R}_d$, a time step, $\Delta t = 0.015R_d/U_0$, and $R = U_0R_d^3/\nu = 5800$, where ν is the biharmonic momentum diffusion coefficient.

Lagrangian floats within the model are advected according to


$$\frac{d(x, y)}{dt} = (u, v), \quad (\text{A1})$$

solved using a fourth-order Runge–Kutta scheme. The velocities were estimated within a grid box using a four-point bilinear interpolation from the box’s corners. We also used a nine-point nonlinear interpolation for comparison and found very little difference. We initialized the model with 21 zonal lines of floats symmetrically distributed about $y = 0$, and separated by $0.3R_d$ from each other. Each line of floats contained forty equally spaced floats.

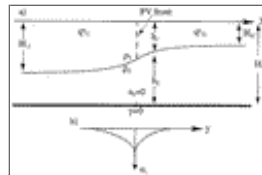
To compute the mean tracer evolution we added to [Hallberg’s \(1995\)](#) model a tracer (χ) advection–diffusion equation solver for $D\chi/Dt = \kappa\nabla^2\chi$, with a constant diffusivity κ , using an operator splitting method ([Press et al. 1992](#)). Advection is performed using a positive definite tracer advection scheme ([Easter 1993](#)) and diffusion by a finite difference explicit scheme. No-flux boundary conditions were applied at the channel’s walls. The explicit tracer diffusivity κ was varied from 0 to $1000 \text{ m}^2 \text{ s}^{-1}$ to assess its effect on mixing.

In addition to the explicit tracer diffusivity (κ), there is an implicit numerical diffusion in the numerical model (κ_{num}). This diffusion can be either positive or negative, varies with both time and space, and is strongest where the advective velocity is perpendicular to the tracer gradient. Dimensional and numerical analysis suggest that

$$\kappa_{\text{num}} \propto \frac{|\mathbf{u} \cdot \nabla \chi| (\Delta x)^2}{\chi_o}, \quad (\text{A2})$$

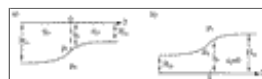
where χ_o is a representative tracer concentration. The theoretical maximum of the numerical diffusivity $\max(\bar{u}) \cdot \Delta x$ occurs if a strong $O(\chi_o)$ discontinuity in tracer concentration exists over a grid point perpendicular to the maximum in jet velocity (the gradient is *parallel* to the flow). Here, we initialize the model with a concentration gradient *perpendicular* to the advection velocity, with a gradient less than 0.01 tracer units per grid point. The tracer is advected by the modeled flow velocities, and its gradient is expected to stay largely *perpendicular* to the direction of the flow. We therefore expect that $\kappa_{\text{num}} \ll 10 \text{ m}^2 \text{ s}^{-1}$ (e.g., [Fig. 10](#) ). The small sensitivity of the tracer fields to variation in Δx (not shown) affirmed this point.

Figures



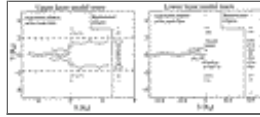
[Click on thumbnail for full-sized image.](#)

Fig. 1. Schematic of the (a) depth and (b) velocity fields of an upper-layer potential vorticity front. The upper-layer flow is geostrophic and has piecewise constant PV, $q^0_{1j} = f/H_{1j}$, where j denotes the side of the front (1 being south, $y < 0$), H_{1j} denotes the depth of the upper layer at $y \rightarrow \pm\infty$, respectively, and the lower layer is quiescent. When $H_{12} = 0$, the interface between the layers intersects the surface, resulting in an outcropping front.



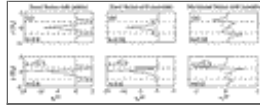
[Click on thumbnail for full-sized image.](#)

Fig. 2. The (a) upper and (b) lower 1½-layer models are used to interpret the instabilities present in the two-layer model of Fig. 1. The jet structure of the upper-layer model is identical to that of the two-layer model. Both 1½-layer models are stable to normal-mode perturbation, while the two-layer model is unstable.



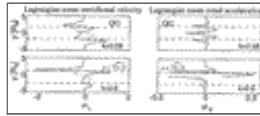
Click on thumbnail for full-sized image.

Fig. 3. Particle trajectory relative to the basic-state flow (left side of each panel) and the displacement ellipses (right side of each panel) for the first vortical modes of the upper and lower 1½-layer QG models ($k = 0.6$). Particles were initially at $x = 0$ and drifted for two periods. All displacements are normalized by $\mu'_n(y = 0)$. Broken lines denote the positions of critical lines of the upper 1½-layer model (where $u^0_1 = c$).



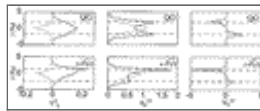
Click on thumbnail for full-sized image.

Fig. 4. Stokes drifts of both stable (left panels) and unstable (center and right panels) flows. Results are shown for QG PV front and an intermediate ϵ PV front. Solid (dashed) lines represent upper (lower) layer variables and broken lines denote both the position of the critical lines in the upper layer (where $u_1 = \text{Re}\{c\}$) and the position of the outcropping front. The Stokes drifts are normalized by a^2 where $a \equiv [2\max(\mu_n(0))]/\lambda$ for the stable waves (modes of Fig. 2). For the unstable waves (modes of Fig. 4), $a \equiv [2\max(\mu_1(0))]/\lambda$.



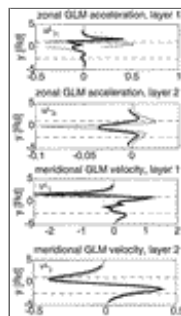
Click on thumbnail for full-sized image.

Fig. 5. The upper-layer (solid line) and lower-layer (dotted line) meridional GLM velocity (U^L_n , left panels) and zonal acceleration (u^L_{nt} ; right panels), for a QG PV front (with $\epsilon = 0.71$) and SW PV front with the same ϵ . Each was normalized as in Fig. 4. Broken lines denote the positions of critical lines (where $u^0_1 = \text{Re}\{c\}$) and the position of the outcropping front.



Click on thumbnail for full-sized image.

Fig. 6. The upper-layer (solid line) and lower-layer (dotted line) Eulerian mean meridional tracer velocity (U^T_n , left panels), eddy diffusivity (κ^{yy}_n , center panels), and horizontal displacement cross-correlation (κ^{xy}_n ; left panel) for a QG PV front (with $\epsilon = 0.71$) and SW PV front with the same ϵ . All are normalized as in Fig. 4. Broken lines denote the positions of critical lines (where $u^0_1 = \text{Re}\{c\}$) and the position of the outcropping front.



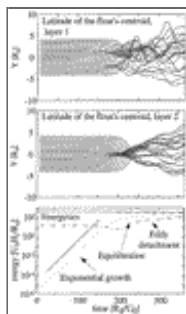
Click on thumbnail for full-sized image.

Fig. 7. Meridional GLM velocity and zonal acceleration in the upper and lower layers in theory (thin lines) and in the numerical model (thick lines), both with intermediate $\epsilon = 0.71$. All are normalized with a^2 where $a = 0.15 \pm 0.02$ in the model. Dashed lines denote the position of the theoretical critical lines in layer 1.



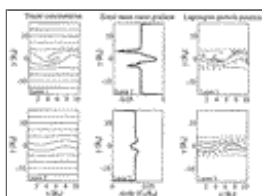
[Click on thumbnail for full-sized image.](#)

Fig. 8. Time rate of change of zonal mean tracer concentration divided by the zonal mean gradient as predicted by theory (thin line) and as calculated from the numerical model results (thick line) in both layers. All are normalized by a^2 , where $a = [2 \max(\mu_1(0))]/\lambda$; $a = 0.05 \pm 0.01$ for the model run with $\kappa = 0$.



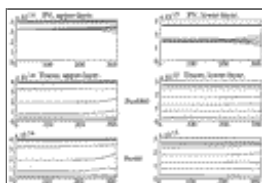
[Click on thumbnail for full-sized image.](#)

Fig. 9. Mean Lagrangian meridional position of the center of gravity of 21 lines of floats, initially spaced evenly around $y = 0$ (upper two panels). In the initial stage of the instability, notice the convergence toward critical lines in the upper layer and toward the center in the lower layer. The evolution of total energy (solid), zonal mean energy (dashed), perturbation energy (dotted), and zonal mean kinetic energy (dot-dashed) as a function of time is shown in the lowest panel. The solid line, parallel to the perturbation energy curve, represents the theoretical growth rate of the instability, $\exp(2\omega_p t)$.



[Click on thumbnail for full-sized image.](#)

Fig. 10. Tracer field (left panels, with 10 contours of values equally spaced between 0 and 1), zonal mean meridional tracer gradients (center panels), and position of Lagrangian floats (right panels). Floats were initially aligned parallel to the PV front at a distance of 1.2 (\circ), 2.4 (\times), and 3.9 ($+$) deformation radii on both the north and south sides of the front. Solid line denotes the position of the PV front. The tracer fields were calculated at $t = 188$ with tracer diffusivity $\kappa = 10 \text{ m}^2 \text{ s}^{-1}$ in the upper (upper panels) and lower (lower panels) layers. Notice the fluid convergence pattern in the lower layer (lower left and right panels) and both pooling and recirculation in the upper layer (upper left and right panels) in both tracer field and Lagrangian particles' position.



[Click on thumbnail for full-sized image.](#)

Fig. 11. Time evolution of the volume of PV and tracer bins. The volume in each bin is represented by the distance between two consecutive lines, from lower values up, with the bold line denoting the total cumulative volume in all the bins, which is constant. For example, the volume in the fourth bin ($0.5 < \theta < 0.7$) is given by the distance between the fourth and third lines from the bottom. Change in the distance between two lines denotes conversion of water and hence net mixing. Tracer volumes are given for $\text{Pe} = 60$ and 6000 .

¹ *Critical level* denotes the position, in the vertical, where downstream mean flow speed equals phase speed ($u^0 = c$). *Critical line* denotes the horizontal position in a layered flow where $u^0 = c$. In continuously stratified flows with variations in the horizontal, $u^0 = c$ defines a two-dimensional *critical* (or *steering*) *surface* (Pratt et al. 1995).

² *Stirring* refers to dispersion of parcels from each other (divergence) and the deformation of material lines in an inviscid model. *Mixing* implies changes in properties of parcels due to interaction with surrounding fluid.

³ Vertical velocities in this section are evaluated at the interface $z = h_1^0$ and are defined to be positive upward. They decay to zero at the top and bottom boundary, are equal at the interface, and are included here for comparison with the results of both Shepherd (1983) and continuously stratified models (AHL).

⁴ We compute the zonal Lagrangian acceleration because it is proportional to the wave induced $O(a^2)$ part of the Lagrangian velocity $u_{nt}^L = 2\omega_f(\tilde{\mathbf{u}}_n + u_n^{SD})$ and for comparison with floats trajectory data from the numerical model. To recover the GLM zonal velocity, use $u_n^L = u_n^0 + u_{nt}^L/(2\omega_f)$.

Corresponding author address: Dr. Emmanuel Boss, COAS, Oregon State University, 104 Ocean Admin. Bldg, Corvallis, OR 97331-5503.

E-mail: boss@oce.orst.edu

top ▲



© 2008 American Meteorological Society [Privacy Policy and Disclaimer](#)
Headquarters: 45 Beacon Street Boston, MA 02108-3693
DC Office: 1120 G Street, NW, Suite 800 Washington DC, 20005-3826
amsinfo@ametsoc.org Phone: 617-227-2425 Fax: 617-742-8718
[Allen Press, Inc.](#) assists in the online publication of AMS journals.